Cascaded-Systems Analysis of Flat-Panel Sandwich Detectors for Single-Shot Dual-Energy X-ray Imaging

Ho Kyung Kim [a,b*], Dong Woon Kim [a], Junwoo Kim [a], Hanbean Youn [b]
[a]*School of Mechanical Engineering, Pusan National University, Busan 609-735*
[b]*Center for Advanced Medical Engineering Research, Pusan National University, Busan 609-735*
[*]*Corresponding author: hokyung@pusan.ac.kr*

1. Introduction

Commercial dual-energy imaging systems employing flat-panel detectors (FPDs) use a dual-shot approach that acquires low- and high-energy projections in successive x-ray exposures by rapidly switching the kilovoltage (kV) applied to the x-ray tube. Receiver-operating characteristic studies have shown that this dual-energy method can improve conspicuity of lesions in particular examination, such as the detection and characterization of small lung lesions, compared to conventional digital radiography for the same patient dose [1]. However, the time interval between exposures can result in motion artifacts that must be addressed [2]. Therefore, reduction of motion artifacts is a priority in the development of new dual-energy x-ray imaging methods.

In previous studies [3,4], we suggested a single-shot (single-kV) method using a novel flat-panel sandwich-style (multi-layer) detector that is insensitive to motion artifacts as described in Fig. 1. The front FPD absorbs low-energy x-ray photons while the rear FPD absorbs high-energy photons. While this single-shot method is more tolerant of object or patient motion and less susceptible to motion artifacts, it generally suffer from reduced contrast-to-noise ratio (CNR) compared to the dual-shot method for the same total patient dose due to poor spectral separation (i.e. ΔE as designated in Fig. 1) [4,5,6]. In addition, particular attention should be given to the signal and noise implications of x-ray photons that may interact directly in the photodiode arrays with the sandwich design, as schematically illustrated in Fig. 1.

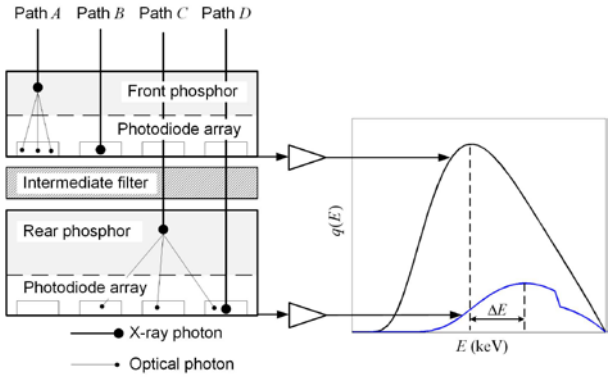

Fig. 1. Schematic illustration of signal detection in the flat-panel sandwich detector and the spectra measured from the front and rear detectors.

The objective of this study is to develop a cascaded-systems model describing signal and noise propagation in the flat-panel sandwich detector. The model includes direct interaction of x-ray photons in active photodiode regions that is unavoidable in the sandwich detector design with a corresponding potential increase in image noise. The developed cascaded-systems model is validated in comparison with the experimental measurements.

2. Methods and Results

2.1 Flat-Panel Sandwich Detectors

Sandwich-style single-shot detector was developed by stacking two FPDs [3,4]. Each FPD consisted of a commercially-available terbium-doped gadolinium oxysulfide (Gd_2O_2S:Tb) scintillator optically coupled to a complementary metal-oxide semiconductor (CMOS) matrix-addressed photodiode array (RadEye1™, Teledyne Rad-icon Imaging Corp., Sunnyvale, CA). The CMOS sensor had 0.048-mm pixels arranged in a 1024 × 512 format to provide an imaging area of approximately 50 × 25 mm. A thin copper (Cu) sheet was placed between the two FPDs to improve spectral separation. The sandwich detector was installed in a light-tight aluminum (Al) box with a 1-mm thick polycarbonate entrance window. To obtain specific material-enhanced images with high contrast, it is crucial to determine the optimal combination between the front and rear scintillators in terms of thickness and optical design. For example, the rear scintillator would be thicker to achieve high quantum efficiency for the higher-energy spectrum.

2.2 Cascaded-Systems Model

With the sandwich configuration, direct interaction of x-ray photons in photodiode active regions are possible, with a corresponding potential increase in image noise [7,8] as illustrated in Fig. 1. We accommodated signal and noise from these direct interactions in the cascaded model as illustrated in Fig. 2. Path *A* describes conversion of x-ray quanta to light quanta in the front phosphor and their detection in the front photodiode array, the normal process in indirect-conversion phosphor-based FPDs, where α_{scn}^{F} is the probability of x-ray interaction in the front screen, β_{scn}^{F} is the

conversion gain to optical quanta (considering the optical collection at the detector), T_{scn}^{F} is the modulation-transfer function (MTF) of the front screen, and α_{pd}^{F} is the probability of an optical photon liberating a charge pair in the silicon (Si) photodiode (i.e. optical quantum efficiency of the detector). The subsequent integral represents the integration of all liberated charges in the detector element, followed by sampling and addition of readout noise. Path *B* describes detection of charge pairs liberated by direct interactions in the photodiode array. Of the fraction $1-\alpha_{scn}^{F}$ of incident x-ray quanta that do not interact in the front phosphor, a fraction α_{pd}^{F} interacts directly in the photodiode, liberating β_{pd}^{F} charge pairs with each interaction. The charge-pair spreading is characterized by T_{pd}^{F}. Of the x-ray photons that pass through the front detector, a fraction $1-\alpha_{IF}$ passes through the Cu filter. Path *C* describes charge pairs liberated in the rear detector from x-ray interactions in the rear phosphor and path *D* describes direct x-ray interactions in the rear photodiode. In general, statistical correlations may exist between parallel cascades requiring the use of cross terms in the noise variance. However, in this model each hexagon represents a quantum branch process and the cross terms are all zero. This happens because incident x-ray quanta are all statistically independent and the signal from any one x-ray photon does not contribute to more than one path.

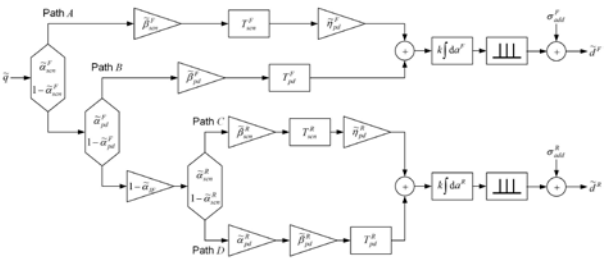

Fig. 2. Cascade-model block diagram describing signal and noise propagation in the flat-panel sandwich detector.

Then, the detective quantum efficiency (DQE) of the *i*-th layer detector as a function of spatial frequency *u* can be given by

$$\mathrm{DQE}^{i}(u)=\frac{\left[T_{scn}^{i}(u)\mathrm{sinc}(au)\right]^{2}}{W_{cor}^{i}(u)+W_{direct}^{i}(u)+W_{add}^{i}(u)}, \tag{1}$$

where the normalized noise-power spectrum (NNPS) terms are:

$$W_{cor}^{i}(u) = \left(\frac{m_{scn}^{i}}{g^{i}}\right)^{2}\left[\frac{1}{\gamma m_{scn}^{i}}+\frac{1}{\alpha_{scn}^{i}} \times\left(\frac{1}{I_{scn}^{i}}-\frac{1}{\beta_{scn}^{i}}\right)\left(T_{aliased}^{i}(u)\right)^{2}\right], \tag{2}$$

$$W_{direct}^{i}(u)=\frac{\hat{\alpha}_{scn}^{i}}{\gamma\alpha_{pd}^{i}I_{pd}^{i}}\left(\frac{m_{pd}^{i}}{g^{i}}\right)^{2}, \tag{3}$$

and

$$W_{direct}^{i}(u)=\frac{\left(\sigma_{add}^{i}\right)^{2}}{\gamma a^{2}q^{i}\left(g^{i}\right)}. \tag{4}$$

$T_{aliased}^{i}$ implies the aliased MTF after the digital sampling process. $q^{i}=q\tau$ where τ is the transmittance through the front FPD including the filter layer. The detailed descriptions of the developed cascaded model will be given in the meeting.

2.3 Parameter Calculations

In order to analyze the NPS and the DQE of the sandwich detector, we calculated the parameters consisting of the DQE expressions derived in this study as follows:

$$\alpha_{j}^{i}=\frac{\int q^{i}(E)\tilde{\alpha}_{j}^{i}(E)\mathrm{d}E}{\int q^{i}(E)\mathrm{d}E}, \tag{5}$$

$$\begin{aligned}\beta_{j}^{i} &= \frac{\int q^{i}(E)\tilde{\alpha}_{j}^{i}(E)\tilde{\beta}_{j}^{i}(E)\mathrm{d}E}{\int q^{i}(E)\tilde{\alpha}_{j}^{i}(E)\mathrm{d}E} \\ &= \frac{\left\langle\kappa\right\rangle_{t_{j}^{i}}}{w}\frac{\int q^{i}(E)\tilde{\alpha}_{j}^{i}(E)\left\langle\varepsilon(E)\right\rangle\mathrm{d}E}{\int q^{i}(E)\tilde{\alpha}_{j}^{i}(E)\mathrm{d}E},\end{aligned} \tag{6}$$

and

$$I_{j}^{i}=\frac{\left(\beta_{j}^{i}\right)^{2}}{\left\langle\left(\beta_{j}^{i}\right)^{2}\right\rangle}=\frac{M_{1}^{2}}{M_{0}M_{2}}. \tag{7}$$

The detailed descriptions of the calculation algorithm will be presented in the meeting.

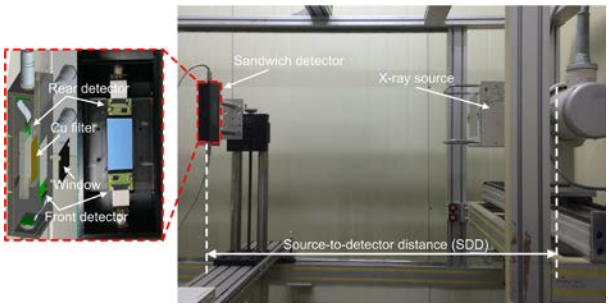

Fig. 3. Photograph of the experimental setup for the measurements of imaging characteristics of the flat-panel sandwich detector. Inset shows a CAD drawing and photograph of the sandwich detector.

2.4 Experimental

Imaging performance, such as MTF, NPS, and DQE, of the flat-panel sandwich detector was characterized by using a 60-kV tungsten-anode spectrum (E7239, Toshiba, Japan). The measured half-value layer (HVL) was 2.4 mm of Al. A source-to-detector distance of 1 m was used and the detector-entrance exposure was

measured by replacing the detector with a calibrated ion chamber (Piranha^{TM} R&F/M 605, RTI Electronics AB, Sweden). From the x-ray spectral simulation for the applied kV and measured HVL, we determined $q_0 = q/X = 1.6 \times 10^5$ photons mm^{-1} mR^{-1}, where X designates exposure in units of mR. Figure 3 represents the experimental setup.

The detector response as a function of exposure was analyzed in a central 128 × 128 pixel region of images. The MTF was estimated from a finely sampled line-spread function, obtained by differentiating the slanted edge images. The NPS was determined using a two-dimensional (2D) Fourier analysis of 128 × 128 pixel region of images. The 1D NPS was extracted from the 2D NPS in the radial direction. Fifteen images were used for each analysis at each exposure level and the typical gain-offset correction procedure was applied to all images before analysis.

Readout of the detector was not synchronized with the x-ray pulse duration. Instead, the detector was operated with an integration time of 3 s long enough to cover all x-ray irradiation time. Since the detector readout noise is proportional to the integration time, we expect that the images contain the detector readout noise larger than that obtained during x-ray irradiation time.

The detector readout noise was estimated from the subtracted images between two dark images. We divided the standard deviation analyzed from the subtracted image by $\sqrt{2}$ and converted the analog-to-digital units (ADUs) into units of the number of electrons by using the conversion factor of 500 e^-/ADU [9]. The resultant σ_{add} was differently measured according to detector configurations and ranged from ~300 to ~665 e^-.

At the 60-kV spectrum, we obtained postmortem mouse images from the developed flat-panel sandwich detector and generated bone-enhanced images with respect to several exposure levels.

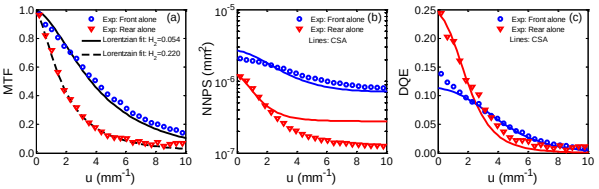

Fig. 4. Summary of the measured results of the signal and noise characteristics in each detector alone comprising the flat-panel sandwich detector: (a) MTF, (b) NNPS (X = ~21 mR), and (c) DQE (~21 mR). In (a), the line curves indicate the Lorentzian fit curves. In (b) and (c), the line curves are the calculation results of the cascaded model developed in this study.

3. Results and Discussion

Imaging performances of each detector alone comprising the sandwich detector are summarized in Fig. 4. Since a thicker phosphor was used, the rear detector alone showed the lower MTF and the better NNPS performances than the front detector alone. Although some discrepancy between the CSA and the measured NNPS of the rear detector alone at frequencies greater than ~2 mm^{-1} was observed as shown in Fig. 4(b), the developed cascaded model reasonably described the measured data.

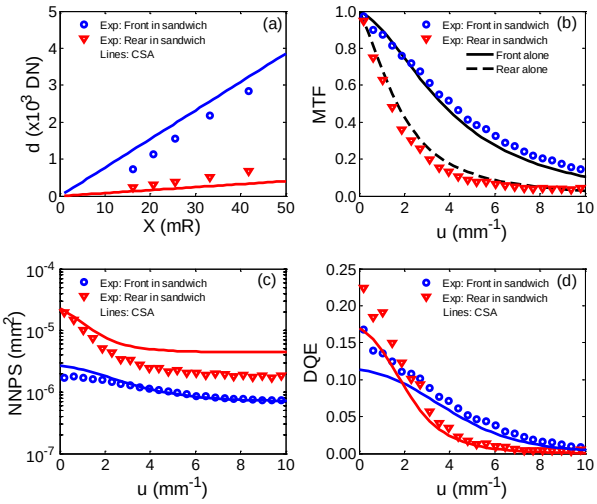

Fig. 5. Summary of the measured results of the signal and noise characteristics in the flat-panel sandwich detector: (a) detector response, (b) MTF, (c) NNPS (X = ~21 mR at the front detector surface), and (d) DQE (~21 mR at the front detector surface). In (a), (c), and (d), the line curves are the CSA results. In (b), the line curves indicate the Lorentzian fit curves obtained from the front and rear detector alone geometries.

Figure 5 summarizes the imaging performances of the sandwich detector and also includes the CSA results. As expected, the detector response at the rear detector even with a thicker phosphor layer is substantially lower than that at the front detector as plotted in Fig. 5(a).

Measured MTFs of the front and rear detectors in the sandwich configuration are shown in Fig. 5(b). The Lorentzian MTF models obtained from each-detector-alone configuration are also over-plotted, and the MTFs of the front and rear detectors in the sandwich configuration are almost the same as those of each-detector-alone configuration.

Figure 5(c) compares the measured and calculated NNPSs. As shown in Fig. 6, the measured NNPS at the rear detector in the sandwich configuration can be reasonably addressed by the component CSA. All the NNPS components at the rear detector in the sandwich configuration were increased compared with those in the rear-detector-alone configuration. Due to the transmittance factor of τ the increase of additive electronic NNPS was most significant.

Consequently, the DQE of the rear detector in the sandwich configuration was degraded compared with that in the rear-detector-alone configuration, as shown in Fig. 5(d). The difference between the measured and calculated τ values (~0.063 and 0.079, respectively) affected the discrepancy between the measured and

calculated NNPS and DQE performances of the rear detector in the sandwich configuration.

The detailed CSA of the NNPS of the rear detector in the separate and the sandwich configurations is shown Fig. 6.

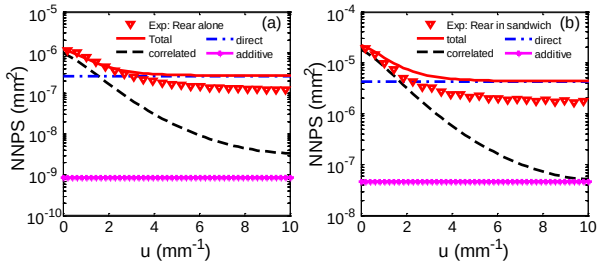

Fig. 6. Cascaded-systems analysis of the NNPS of the rear detector measured in (a) the separate and (b) sandwich configurations.

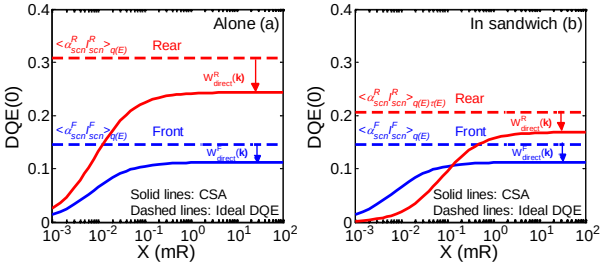

Fig. 7. Cascaded-systems analysis of the DQE(0) as a function of exposure: (a) each detector alone and (b) sandwich configurations.

Figure 7 shows the CSA results on exposure dependencies of the DQE at zero frequency or DQE(0) of each detector layer in its alone and in the sandwich configurations. In this analysis, we assumed that additive electronic noise is the same for all the detector layers as 500 e^-. It is also noted that the exposure reading the axis of abscissa in Fig. 7(b) is the exposure at the front detector entrance surface of the sandwich detector. Therefore, the exposure on the rear detector is lowered by a factor of τ (= ~0.07 in this study) considering the transmission through the front detector layer including the Cu filter. Regardless of detector configurations, the DQE(0) increased with increasing exposure, and then saturated. This is because the effect of additive electronic noise on DQE is canceled out at higher exposures, and is typically known behavior in the flat-panel detector operation. In this study, we define the exposure level at which the DQE approaches 90% of its maximum value as the quantum-noise-limited exposure X_{limit}. In the separate detector configurations, both the front and the rear detector alone showed the same X_{limit} of ~8×10^{-2} mR, as shown in Fig. 7(a). X_{limit} of the front detector was unchanged when it operated as the sandwich detector, whereas X_{limit} of the rear detector in the sandwich configuration was increased by a factor of ~10 compared with its alone configuration because of the reduced incident fluence on the rear detector, as shown in Fig. 7(b). The difference between the transmission factor and the reduction factor in X_{limit} of the rear detector could be explained by the scatter photon effects.

The ideal DQE(0) can be determined by multiplication of quantum efficiency and the Swank factor [10]. As shown in Fig. 7(a), the DQE(0) values of the front and rear detectors in their separate configurations never reached their ideal values; 77 and 79% of the ideal DQE(0) values, respectively. The reason is the additional noise, called “direct x-ray interaction noise” introduced in this study. The effect of direct x-ray interaction noise on the DQE performance was reduced by ~3% for the rear detector when it operated as the sandwich detector, as shown in Fig. 7(b).

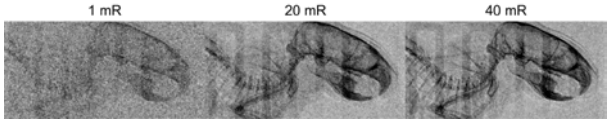

Fig. 8. Comparison of bone-enhanced postmortem mouse images obtained from the single-shot flat-panel sandwich detector with a 0.3 mm-thick Cu filter with respect to various exposures measured at the front detector entrance surface.

Figure 8 shows single-shot dual-energy bone images of a postmortem mouse using the flat-panel sandwich detector for several exposure levels measured at the front layer. The overall image quality was dependent upon the exposure level. Correlation between image quality (e.g. SNR and CNR) and the system DQE performance with respect to various exposures will be investigated in a next study.

4. Conclusions

We have developed the cascaded-systems model to investigate the signal and noise characteristics in the flat-panel sandwich detector which was developed for the preclinical single-shot dual-energy x-ray imaging. The model incorporates parallel branches to include direct interaction of x-rays in photodiode that is unavoidable in the sandwich structure with a corresponding potential increase in image noise. The model has been validated in comparison with the experimental. The cascaded-systems analysis shows that direct x-ray interaction noise behaves as additive electronic noise that is white in the frequency domain; hence it is harmful to the DQE at higher frequencies where the number of secondary quanta lessens. Even at zero frequency, the direct x-ray interaction noise can reduce the DQE of the detectors investigated in this study by ~20% for the 60 kV x-ray spectrum. The DQE of rear detector in the sandwich structure is sensitive to additive electronic noise because of the enhancement in the number of electronic noise quanta relative to that of x-ray quanta that are attenuated through the front layers including the intermediate filter layer (i.e. incident photon fluence times transmission factor). To operate the rear layer of the sandwich detector in the quantum-noise-limited region, exposure as higher as the

transmission factor is required compared with when the detector is used as a separate single layer in the quantum-noise-limited region. Otherwise, the rear detector should be designed to have a larger gain factor than the front detector by a factor of the reciprocal square root of the transmission factor. The cascaded model developed in this study will be very useful for exploring the optimal design of sandwich detector and imaging technique with it.

ACKNOWLEDGMENTS

This work was supported by the National Research Foundation (NRF) grants funded by the Korea government (MSIP) (No. 2014R1A2A2A01004416 and No. 2013M2A2A9046313).

REFERENCES

[1] H. Kashani, C. A. Varon, N. S. Paul, G. J. Gang, R. V. Metter, J. Yorkston, and J. H. Siewerdsen, Diagnostic performance of a prototype dual-energy chest imaging systems: ROC analysis, Academic Radiology, Vol.17, p. 298, 2010.
[2] N. A. Shkumat, J. H. Siewerdsen, A. C. Dhanantwari, D. B. Williams, N. S. Paul, J. Yorkston, and R. V. Metter, Cardiac gating with a pulse oximeter for dual-energy imaging, Physics in Medicine and Biology, Vol.53, p.6097, 2008.
[3] S. Yun, J. C. Han, D. W. Kim, H. Youn, H. K. Kim, J. Tanguay, and I. A. Cunningham, Feasibility of active sandwich detectors for single-shot dual-energy imaging, Proceedings of SPIE, Vol.9033, p.90335T, 2014.
[4] J. C. Han, H. K. Kim, D. W. Kim, S. Yun, H. Youn, S. Kam, J. Tanguay, and I. A. Cunningham, Single-shot dual-energy x-ray imaging with a flat-panel sandwich detector for preclinical imaging, Current Applied Physics, Vol.14, p.1734, 2014.
[5] R. E. Alvarez, J. A. Seibert, and S. K. Thompson, Comparison of dual energy detector system performance, Medical Physics, Vol.31, p.556, 2004.
[6] S. Richard and J. H. Siewerdsen, Optimization of dual-energy imaging systems using generalized NEQ and imaging task, Medical Physics, Vol.34, p.127, 2007.
[7] H. K. Kim, Generalized cascaded model to assess noise transfer in scintillator-based x-ray imaging detectors, Applied Physics Letters, Vol.89, p.233504, 2006.
[8] S. Yun, H. K. Kim, C. H. Lim, M. K. Cho, T. Achterkirchen, and I. Cunningham, Signal and noise characteristics induced by unattenuated x rays from a scintillator in indirect-conversion CMOS photodiode array detectors," IEEE Transactions on Nuclear Science, Vol.56, p.1121, 2009.
[9] J. C. Han, S. Yun, C. H. Lim, T. W. Kim, and H. K. Kim, "Feasibility study of CMOS detectors for mammography, Proceedings of SPIE, Vol.7258, p.72583I, 2009.
[10] H. K. Kim, Practical expressions describing detective quantum efficiency in flat-panel detectors, Journal of Instrumentation, Vol.6, p.C11020, 2011.